AIAA JOURNAL
Vol. 47, No. 5, May 2009

Receptivity of a Supersonic Boundary Layer to Acoustic Disturbances

P. Balakumar*
NASA Langley Research Center, Hampton, Virginia 23681

DOI: 10.2514/1.33395

The boundary layer receptivity process generated by the interaction of 3-D slow and fast acoustic disturbances with a blunted flat plate, is numerically investigated at a freestream Mach number of 3.5, and at a high Reynolds number of $39 * 10^6$/m. The computations are performed with and without a 2-D isolated roughness element located near the leading edge. Both the steady and unsteady solutions are obtained by solving the full Navier-Stokes equations using the fifth-order accurate weighted essentially nonoscillatory scheme for space discretization and using the third-order total-variation-diminishing Runge-Kutta scheme for time integration. The simulations showed that the linear instability waves are generated very close to the leading edge. The wavelength of the disturbances inside the boundary layer first increases gradually and becomes longer than the wavelength for the instability waves within a short distance from the leading edge. The wavelength then decreases gradually and merges with the wavelength for the Tollmien-Schlichting wave. The initial amplitudes of the instability waves near the neutral points, the receptivity coefficients, are about 1.20 and 0.07 times the amplitude of the freestream disturbances for the slow and fast waves, respectively. It was also revealed that a small isolated roughness element does not enhance the receptivity process for the given nose bluntness.

Nomenclature

a	=	major axis of the ellipse
b	=	minor axis of the ellipse
C_{recpt}	=	receptivity coefficient
E	=	total energy
e	=	internal energy
F	=	nondimensional frequency
F_{ij}	=	inviscid fluxes
F_{vij}	=	viscous fluxes
f	=	frequency in Hertz
f_r	=	shape of the roughness
h	=	height of the roughness
J	=	Jacobian
k	=	thermal conductivity
M	=	Mach number
Pr	=	Prandtl number
p	=	pressure
Q	=	conserved variable vector
q	=	heat flux
Re	=	Reynolds number
T	=	temperature
t	=	time
u, v, w	=	velocity components
x, y, z	=	Cartesian coordinates
x_b	=	roughness location
α	=	streamwise wave number
β	=	spanwise wave number
δ	=	boundary-layer thickness
ξ, η, ζ	=	Coordinates in transformed plane
μ	=	viscosity
ρ	=	density
σ	=	parameter in the roughness function
τ	=	shear stress
ν	=	kinematic viscosity
ω	=	frequency
$(.)_{\text{ac}}$	=	acoustic disturbance
$(\sim)$	=	amplitude of the fluctuations
$(.)'$	=	fluctuating quantity
$(.)_\infty$	=	freestream value

Presented as Paper 0096 at the 43rd AIAA Aerospace Sciences Meeting and Exhibit, Reno, Nevada, 10–13 January 2005; received 12 July 2007; revision received 6 January 2009; accepted for publication 23 January 2009.

*Aerospace Engineer, Flow Physics and Control Branch, Mail Stop 170. Member AIAA.

I. Introduction

TRANSITION from a laminar to a turbulent state in shear flows occurs due to the evolution and interaction of different disturbances inside the shear layer. Though there are several mechanisms and routes to go from a laminar to a turbulent state, most of them generally follow these fundamental processes: 1) receptivity; 2) linear instability; 3) nonlinear instability and saturation; and 4) secondary instability and breakdown to turbulence.

In the receptivity process, unsteady disturbances in the environment such as acoustics and turbulence interact with the inhomogeneities in the geometry, such as roughness, and generate instability waves inside the shear layer. In quiet environments, the initial amplitudes of these instability waves are small compared to any characteristic velocity and length scales in the flow. In the second stage, the amplitudes of these instability waves grow exponentially downstream and this process is governed by the linearized Navier-Stokes equation. Further downstream, the amplitudes of the disturbances become large, the nonlinear effects inhibit the exponential growth, and the amplitude of the waves eventually saturate. In the next stage, the finite amplitude saturated disturbances become unstable to 2-D and/or 3-D disturbances. This is called secondary instability, and beyond this stage the spectrum broadens due to complex interactions and further instabilities, and the flow becomes turbulent in a short distance downstream. In a previous study [1], the interactions of 2-D acoustic disturbances with isolated 2-D roughness elements in a supersonic boundary layer were investigated. It was found that isolated roughness does not enhance the generation of disturbances compared to that generated by acoustic disturbances. Since the 2-D instability waves are almost neutral, it was difficult to discern between the evolution of the forced continuous spectrum and the instability waves. In this paper, the generation and evolution of 3-D disturbances induced by acoustic disturbances and isolated roughness in a supersonic boundary layer with a freestream Mach number of 3.5 is investigated.

Accurately predicting transition onset and transition end points and modeling the transitional and turbulence regions are the major difficulties in using CFD codes to compute aerodynamic quantities. Our understanding of different instability mechanisms and different transition processes in shear layers have greatly improved in the last several decades [2,3]. However, transition prediction methods have not made much progress. The main difficulty is due to the nature of the transition process itself. The transition process mainly depends on the boundary-layer characteristics and on the frequency and wave number distributions of the disturbances that enter the boundary layer. The laminar boundary-layer profiles can be computed easily. The problem is computing, predicting, or prescribing the initial spectral, amplitude, and phase distribution of the disturbances inside the boundary layer. The initial disturbances are generated by the interaction of the freestream unsteady disturbances and the roughness on the surface. These two are stochastic in nature and are difficult to quantify in general. In any new transition prediction strategy, one should quantify these two quantities and should determine what is the minimum amount of information necessary to predict the transition onset accurately. The objectives of this research work are to answer some of these questions and eventually to come up with an improved transition prediction method.

There have been numerous investigations conducted on the interaction of acoustic waves with supersonic boundary layers. The interactions of acoustic waves with a supersonic boundary layer at finite incident angles using inhomogeneous stability equations are investigated in [4,5]. Because of the interaction, one important finding showed that acoustic waves excite disturbances inside the boundary layer that are much larger than those in the freestream. The interaction of streamwise acoustic waves with a nonparallel boundary layer was studied in [6]. The analysis and the calculations showed that the disturbances inside the boundary layer reach significant values compared with those in the outside. It was also observed that there exists a critical Reynolds number where this excitation is the highest. Fedorov and Khokhlov [7] investigated using asymptotic theory of the excitation of the first and second modes by the acoustic waves near the leading-edge region. Gapanov [8] showed that the energy is transmitted to the T-S waves near the critical region where the ratio between the amplitudes of the reflected waves and the incident wave is the largest. Zhong [9], and Ma and Zhong [10] numerically investigated the leading-edge receptivity to 2-D acoustic disturbances for hypersonic flows over a parabola and a flat plate. Egorov et al. [11] investigated the receptivity of a supersonic boundary layer to acoustic disturbances including bluntness effects using asymptotic methods. It is shown that the receptivity coefficient decreases with increasing bluntness at hypersonic Mach numbers. There are not many numerical calculations performed to investigate the interaction of acoustic waves with a flat plate including bluntness at supersonic Mach numbers.

Kendall [12] investigated using hot-wire anemometry of the origin and growth of boundary-layer oscillations in zero pressure gradient boundary layers at supersonic and hypersonic Mach numbers. It was found that the boundary layer fluctuations are well correlated with the freestream acoustic disturbances at higher supersonic Mach numbers. Semionov et al. [13] studied the leading-edge receptivity of a supersonic boundary layer on a flat plate to acoustic disturbances that were radiated from a controlled harmonic source. Maslov et al. [14] experimentally investigated the boundary layer receptivity near a leading edge of a flat plate at hypersonic speeds to acoustic disturbances that were radiated from 2-D and 3-D concentrated sources. These studies showed that the incoming acoustic waves generate the instability waves inside the boundary layer near the leading edge of the plate. There were several relevant transition experiments also performed at NASA Langley in the Mach 3.5 supersonic low-disturbance tunnel. Boundary-layer transition data on a flat plate and on a cone along with freestream noise levels and the power spectral distribution of the freestream noise are presented in [15]. As a first step, the computations are performed for the same conditions as in the experiment. The objectives are to understand the receptivity process near the leading edge of a flat plate and to estimate the receptivity coefficient of the instability waves generated near the leading edge. Computations are also performed to determine whether the slow or fast acoustic modes are more efficient in generating the instability waves and to estimate the effect of the roughness element in generating the instability waves as it interacts with the acoustic waves. To answer these questions the following computations are performed for a supersonic flow over a flat plate with a blunted leading edge: 1) interaction of a 3-D slow acoustic disturbance with the boundary layer; 2) interaction of a 3-D fast acoustic disturbance with the boundary layer; and 3) interaction of a 3-D slow acoustic disturbance with the boundary layer on a flat plate with a 2-D roughness element. A schematic diagram of the computational set up is depicted in Fig. 1.

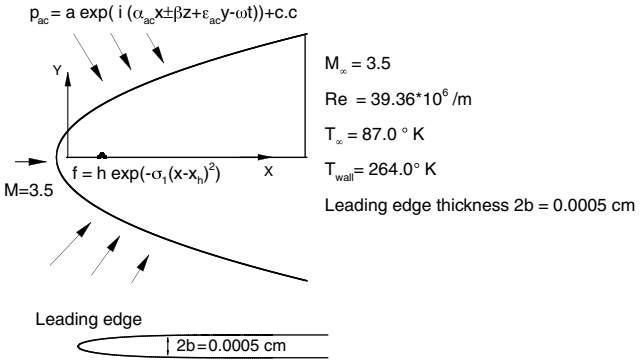

Fig. 1 Schematic diagram of the computational model.

II. Governing Equations

The equations solved are the 3-D unsteady compressible Navier-Stokes equations in conservation form

$$\frac{\partial}{\partial t}Q_i + \frac{\partial}{\partial x_j}(F_{ji} - F_{vji}) = 0 \tag{1}$$

$$\text{Where} \quad Q_i = \begin{Bmatrix} \rho \\ \rho E \\ \rho u \\ \rho v \\ \rho w \end{Bmatrix} [F_{ji}] = \begin{Bmatrix} \rho u_j \\ (\rho E + p)u_j \\ \rho u u_j + \delta_{1j}p \\ \rho v u_j + \delta_{2j}p \\ \rho w u_j + \delta_{3j}p \end{Bmatrix} [F_{vij}]$$

$$= \begin{Bmatrix} 0 \\ u\tau_{1j} + v\tau_{2j} + w\tau_{3j} - q_j \\ \tau_{1j} \\ \tau_{2j} \\ \tau_{3j} \end{Bmatrix} \tag{2}$$

and (x, y, z) are the Cartesian coordinates, (u, v, w) are the velocity components, ρ is the density, and p is the pressure. E is the total energy given by

$$E = e + \frac{u^2 + v^2 + w^2}{2}, \qquad e = c_v T, \qquad p = \rho R T \tag{3}$$

where e is the internal energy and T is the temperature. The shear stress and the heat flux are given by

$$\tau_{ij} = \mu\left\{\frac{\partial u_i}{\partial x_j} + \frac{\partial u_j}{\partial x_i} - \frac{2}{3}\delta_{ij}\frac{\partial u_k}{\partial x_k}\right\}, \qquad q_j = -k\frac{\partial T}{\partial x_j} \tag{4}$$

The viscosity (μ) is computed using Sutherland's law and the coefficient of conductivity (k) is given in terms of the Prandtl number Pr. The variables ρ, p, T, and velocity are nondimensionalized by their corresponding reference variables ρ_∞, p_∞, T_∞ and $\sqrt{RT_\infty}$ respectively. The reference value for length is computed by

$\sqrt{\nu x_0/U_\infty}$, where x_0 is a reference location. For the computation, the equations are transformed from the physical coordinate system (x, y, z) to the computational curvilinear coordinate system (ξ, η, ζ) in a conservative manner and the governing equations become

$$\frac{\partial}{\partial t}\bar{Q}_i + \frac{\partial}{\partial \xi_j}(\bar{F}_{ji} - \bar{F}_{vji}) = 0 \tag{5}$$

The components of the flux in the computational domain are related to the flux in the Cartesian domain by

$$\bar{Q}_i = \frac{Q_i}{|J|}, \qquad [\bar{F}_{ji}] = \frac{J}{|J|}[F_{ji}] \tag{6}$$

where $J = [\frac{\partial(\xi,\eta,\zeta)}{\partial(x,y,z)}]$.

A. Solution Algorithm

The governing equations are solved using a fifth-order accurate weighted essentially nonoscillatory (WENO) scheme for space discretization and using a third order, total-variation-diminishing (TVD) Runge-Kutta scheme for time integration. These methods are suitable in flows with discontinuities or high gradient regions. The governing equations are solved discretely in a uniform structured computational domain where flow properties are known pointwise at the grid nodes. In a given direction, the spatial derivatives are approximated to a higher order at the nodes, using the neighboring nodal values in that direction. The resulting equations are then integrated in time to get the point values as a function of time. Since the spatial derivatives are independent of the coordinate directions, multi dimensions can be easily added to the method. It is well known that approximating a discontinuous function by a higher order (two or more) polynomial generally introduces oscillatory behavior near the discontinuity, and this oscillation increases with the order of the approximation. The essentially nonoscillatory (ENO) method, and the improvement of this, the WENO method, were both developed to maintain the higher order approximations in the smooth regions and to eliminate or suppress the oscillatory behavior near the discontinuities. These are achieved by systematically adopting or selecting the stencils based on the smoothness of the function that is being approximated. Shu [16] explains the WENO and the TVD methods and the formulas. Atkins [17] gives the application of the ENO method to the Navier-Stokes equations. Balakumar et al. [18] describes in detail the solution method implemented in this computation.

At the outflow boundary, characteristic boundary conditions [19] are implemented to obtain the flow variables. At the wall, no-slip conditions are used for the velocities and a constant temperature condition is employed for the temperature. The density at the wall is computed from the continuity equation. In the spanwise direction, symmetric and periodic conditions are used at the boundaries. In the mean flow computations, the freestream values are prescribed at the upper boundary that lies outside the bow shock. In the unsteady computations, the acoustic perturbations are superimposed on the uniform mean flow at the upper boundary. The procedure is to first compute the steady mean flow by performing unsteady computations using a variable time step until the maximum residual reaches a small value $\sim 10^{-11}$. A Courant-Friedrichs-Lewy number of 0.3 is used in these computations. The next step is to introduce unsteady disturbances at the upper boundary of the computational domain and to perform time accurate computations to investigate the interaction and evolution of these disturbances downstream.

The symmetric acoustic field that impinges on the outer boundary is taken to be in the following form:

$$p'_{ac} = \text{Real}\{\tilde{p}_{ac} e^{i\alpha_{ac}x \pm i\beta_{ac}z + i\varepsilon_{ac}y - i\omega t}\} + \text{Real}\{\tilde{p}_{ac} e^{i\alpha_{ac}x \pm i\beta_{ac}z - i\varepsilon_{ac}y - i\omega t}\} \tag{7}$$

Here α_{ac}, β_{ac}, ε_{ac} are the acoustic wave number, and ω is the frequency of the acoustic disturbance. The wave number in the y-direction ε_{ac} determines the incident angle of the acoustic waves, and in this paper computations are performed for zero incident angle, $\varepsilon_{ac} = 0.0$.

To investigate the effect of the roughness element on the transition process, an isolated roughness element of Gaussian shape in the form

$$f_r = he^{-\sigma(x-x_h)^2} \tag{8}$$

is placed at $x = x_h$. Here h is the height of the roughness and σ determines the width of the roughness in the streamwise direction.

III. Results

Computations are performed for a supersonic flow over a semi-infinite flat plate with a blunt leading edge. Table 1 gives the flow parameters and Fig. 1 shows the schematic diagram of the computational setup. The leading edge of the plate is modeled as a super ellipse of the form

$$\frac{(x-a)^4}{a^4} + \frac{y^2}{b^2} = 1 \tag{9}$$

Here b is the thickness of the plate and in accordance with the experiment it is taken as 0.00025 cm (Fig. 9 in [15]). It should be noted that the flat plate in the experiment has a beveled leading-edge angle of 15 deg and the leading-edge radius is 0.00025 cm (Fig. 9 in [15]). The aspect ratio a/b is taken as 10, hence, the blunt leading edge is joined with the straight portion of the plate at $x = 0.0025$ cm., which is at a Reynolds number of 32.0.

The grid is generated using analytical formulas. The grid stretches in the η direction close to the wall and is uniform outside the boundary layer. In the ξ direction, the grid is symmetric about the leading edge, very fine near the nose, and is uniform in the flat region. The grid is uniform in the spanwise direction. The outer boundary

Table 1 Flow parameters for the wind tunnel model

Freestream Mach number: $M_\infty = 3.5$
Freestream Reynolds number: $\text{Re}_\infty = 39.36 * 10^6/\text{m}$
Freestream density: $\rho_\infty = 0.3604\ \text{kg/m}^3$
Freestream pressure: $p_\infty = 8.99$ kPa
Freestream velocity: $U_\infty = 654.02$ m/s
Freestream temperature: $T_\infty = 87.0°\text{K}$
Freestream kinematic viscosity: $\nu_\infty = 1.661 * 10^{-5}\ \text{m}^2/\text{s}$
Wall temperature: $T_\infty = 264.0°\text{K}$
Prandtl number: Pr =0.70
Ratio of specific heats: $\gamma = 1.4$
Length scale $\sqrt{\frac{\nu_\infty x_0}{U_\infty}} = 1.80 * 10^{-3}$ cm ($x_0 = 1.3$ cm)
The boundary-layer thickness at $x = 2.5$ cm: $\delta_0 = 0.0323$ cm
Nondimensional frequency $F = 1 * 10^{-5}$ is equivalent to 41.0 kHz
The nondimensional frequency F is defined as $F = \frac{2\pi\nu_\infty f}{U_\infty^2}$, where f is the frequency in Hertz.
The local Reynolds number Re_x is defined by $\text{Re}_x = \sqrt{\frac{U_\infty x}{\nu_\infty}}$.

that lays outside of the shock follows a parabola with its vertex located a short distance upstream of the leading edge of the plate, Fig. 1. The computational domain extends from $x = -0.038$ to 30.0 cm in the axial direction. Calculations were performed using a grid size (3001*251*11). Because of the very fine grid requirement near the nose, the allowable time step is very small and the computations become very expensive to simulate the unsteady computations in the entire domain. To overcome this, calculations are performed in two steps. First, the computations are done near the nose region with a very small time step. Second, the flow properties in the middle of this domain are fed as inflow conditions for the second larger domain and the computations are carried out with a larger time step. The nose region domain extends up to $x = 1.65$ cm and the second domain starts at $x = 0.76$ cm. Grid refinement studies are performed with different grid distributions near the nose region. Grid 1 is a basic grid of (801*251*11) points with fine grid near the nose and uniform grid in the flat-plate region. Grid 2 is obtained by making the domain in the x and y directions half the size. This grid is finer in the shock region and in the axial direction. Grid 3 is created to make the grid across the shock finer than Grid 2. Grid 4 is the grid used in the computations with the roughness. The grid distribution over the roughness element is shown in [1]. The grid follows the roughness surface and has very fine uniform distribution near $x = 0.25$ cm where the roughness is located.

A. Linear Instability

As a prelude for future reference, in Fig. 2 the linear stability results for the similarity boundary layer over a flat plate is presented. The figure depicts the neutral stability diagram in (Re_x, F) plane for different wave angles 0, 45, 60, and 70 deg. The figure also shows the N-Factor curves and the growth rates for the most amplified disturbances. The critical Reynolds number is about 193 and this occurs for an oblique wave angle of 60 deg. The most amplified frequency is about $F = 1.0$–$1.25 * 10^{-5}$ and the spanwise wave number of the most amplified wave is about $\beta = 0.025$. This corresponds to a wavelength of approximately 0.452 cm and is equivalent to about 14 boundary-layer thicknesses and the most amplified frequency corresponds to about 40–50 kHz. It is also observed that at higher Reynolds numbers $\mathrm{Re}_x > 1000$, only the low frequency disturbances $F < 3.0 * 10^{-5}$ are unstable. This implies that acoustic disturbances with frequencies less than 120 kHz may be the relevant frequency range for generating instability waves inside the boundary layer. Boundary-layer transition data on a flat plate, and freestream noise levels and the power spectral distribution of the freestream noise are presented in [15]. The data shows that the transition Reynolds number for a flat plate in quiet conditions is about $11 * 10^6$. This correlates to an N-Factor of 8.5 at the transition onset point for a constant azimuthal wave number.

Table 2 Values of α_{ac} and wavelength for different sweep angles

β_{ac}	Slow	Fast	Neutral wave
0.0	0.01237 (0.912 cm)	0.00687 (1.64 cm)	0.01225 (0.919 cm)
0.025	0.01757 (0.643 cm)	0.00168 (6.71 cm)	0.01502 (0.752 cm)

B. Acoustic Waves

The solution of linearized Euler equations in a uniform mean flow are:

$$\begin{Bmatrix} \rho \\ u \\ v \\ w \\ T \end{Bmatrix} = \begin{Bmatrix} \frac{1}{a_0^2} \\ -\frac{\alpha_{ac}}{\rho_0(\alpha_{ac}U_0-\omega)} \\ -\frac{\varepsilon_{ac}}{\rho_0(\alpha_{ac}U_0-\omega)} \\ -\frac{\beta_{ac}}{\rho_0(\alpha_{ac}U_0-\omega)} \\ \frac{(\gamma-1)T_0}{\rho_0 a_0^2} \end{Bmatrix} p \tag{10}$$

Here, the pressure p is in the form

$$p = \tilde{p}_{ac} e^{i(\alpha_{ac}x+\varepsilon_{ac}y+\beta_{ac}z-\omega t)} \tag{11}$$

The dispersion relation among the wave numbers α_{ac}, β_{ac}, ε_{ac} and the frequency ω is given by

$$(\alpha_{ac}U_0 - \omega)^2 = (\alpha_{ac}^2 + \beta_{ac}^2 + \varepsilon_{ac}^2)a_0^2 \tag{12}$$

For zero incident angle $\varepsilon_{ac} = 0$, the wave number α_{ac} can be expressed as

$$\alpha_{ac} = \frac{\omega \cos\theta_z}{(U_0 \cos\theta_z \pm a_0)} \tag{13}$$

Here, $\theta_z = \tan^{-1}(\frac{\beta_{ac}}{\alpha_{ac}})$ is the sweep angle, the plus sign corresponds to the fast moving wave, and the minus sign corresponds to the slow moving wave. The corresponding phase speeds are $C = U_0 \pm \frac{a_0}{\cos\theta_z}$. The wave number for the fast moving wave is $\alpha_{ac} < \frac{\omega}{U_0+a_0}$, and for the slow moving wave $\alpha_{ac} > \frac{\omega}{U_0-a_0}$, and the sweep angle is limited by $\theta_z < \cos^{-1}(\frac{1}{M})$. At $M = 3.5$ and $F = 1.25 * 10^{-5}$, the wave numbers of the fast moving and slow moving waves are $\alpha_{ac} < 0.00687$ and $\alpha_{ac} > 0.01237$, and the sweep angle of the slow moving wave is limited to 73.39 deg. The wave numbers and the wavelengths in dimensional units for the slow and the fast acoustic waves and for the neutral stability waves for $\beta_{ac} = 0.0$ and 0.025 are listed in Table 2.

The variation of the wave number α for the instability waves with the Reynolds number Re_x for 2-D $\beta = 0.0$ and 3-D $\beta = 0.025$ instability waves are plotted in Fig. 3. The wave number for the 2-D wave decreases from 0.0124 at a Reynolds number of 220 to 0.0119 at a Reynolds number of 2000. For the 3-D disturbance it decreases from 0.01775 at a Reynolds number of 190 to 0.01285 at a

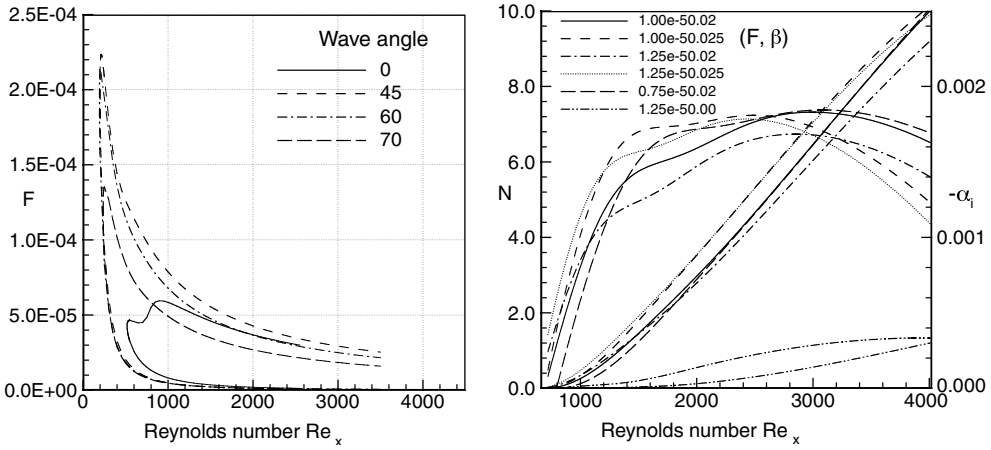

Fig. 2 Stability and N-Factor diagrams for a flat-plate boundary layer. $M_\infty = 3.5$, $T_\infty = 87^\circ$ K.

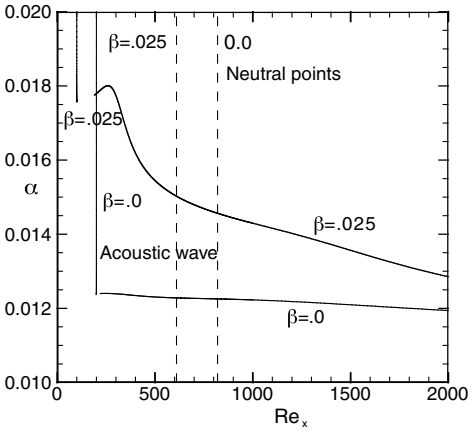

Fig. 3 Variation of the wave number with the Reynolds number for the instability waves and the wave number for the acoustic waves for $\beta = 0.0$ and 0.025.

Reynolds number of 2000. The Reynolds numbers at the neutral points are 820 and 610, respectively, for the 2-D and 3-D disturbances, and they are also marked in Fig. 3. The figure also depicts the range of the acoustic wave numbers α_{ac} for the 2-D and 3-D slow acoustic waves. It is seen that perfect matching in the wave numbers occurs at a very low Reynolds number range where the disturbances are marginally stable. For the unit Reynolds number of $39.36 * 10^6$/m, Reynolds number of 200 is located at 0.10 cm from the leading edge of the plate and the neutral point is located close to $x = 0.91$ cm. Hence, there may be a strong generation of instability waves in the nose region where the bluntness effects and the nonparallel effects will become important.

C. Mean Flow

In Fig. 4, the mean flow density contours computed using the WENO code for both the smooth plate and the plate with an isolated roughness element are shown. Fig. 4a shows the entire domain and Fig. 4b shows the flow field near the nose region. The outer boundary of the leading-edge shock is located approximately 0.000076 cm (0.15b) upstream of the leading edge. Figures 4c and 4d similarly show the density contours of the mean flow with the roughness element. The Mach wave originating from the roughness element propagates parallel to the Mach wave originating from the leading edge. The density profiles for the case without roughness at $x = 0.025, 0.125, 0.635, 1.25, 2.5, 7.6$ cm ($\sqrt{\mathrm{Re}_x} = 100, 224, 500, 707, 1000, 1732$) are plotted in Fig. 5a. Figure 5b shows the same profiles in the similarity coordinates. The Blasius similarity profile is also included for comparison. It is seen that very close to the leading edge, there exists a strong shock, and this compression expands over the leading edge and the shock becomes weaker away from the nose region. The boundary-layer profiles slowly approach the Blasius similarity profiles close to $x = 1.5$ cm.

Figure 6a shows the comparison between the growth rate and N-factors computed using the similarity profiles and the profiles obtained from the numerical simulation for the most amplified wave with $F = 1.25 * 10^{-5}$ and $\beta = 0.025$. Figure 6b shows the second derivative of the temperature for the two mean profiles at the station $x = 12.5$ cm. It is seen that the stability results obtained using the simulation profiles agree reasonably well with that obtained using the Blasius similarity profiles.

D. Interaction of 3-D Acoustic Waves with the Boundary Layer

After the mean flow is obtained, 3-D slow and fast acoustic disturbances are separately introduced at the outer boundaries and time accurate simulations are performed. The nondimensional

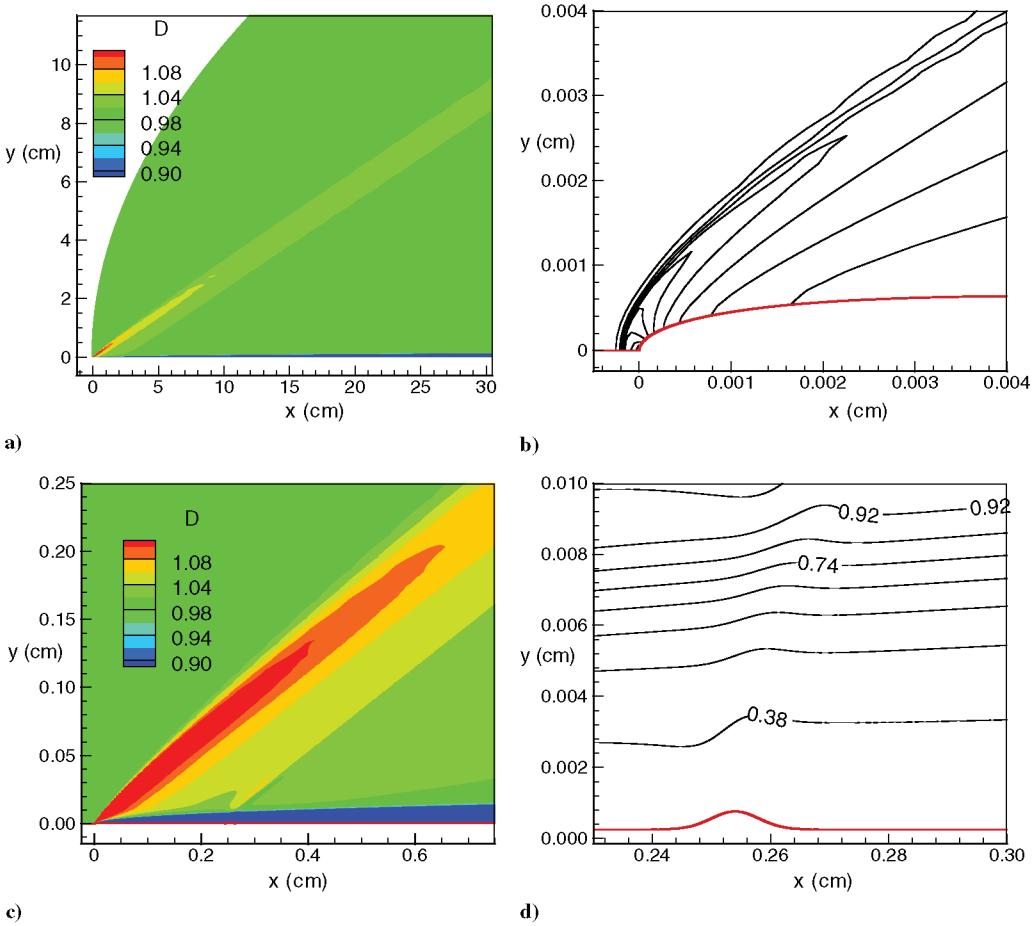

Fig. 4 Contours of the density for flow over a flat plate with a blunted leading edge at $M = 3.5$ with and without roughness. $h = 0.0005$ cm, $x_h = 0.25$ cm.

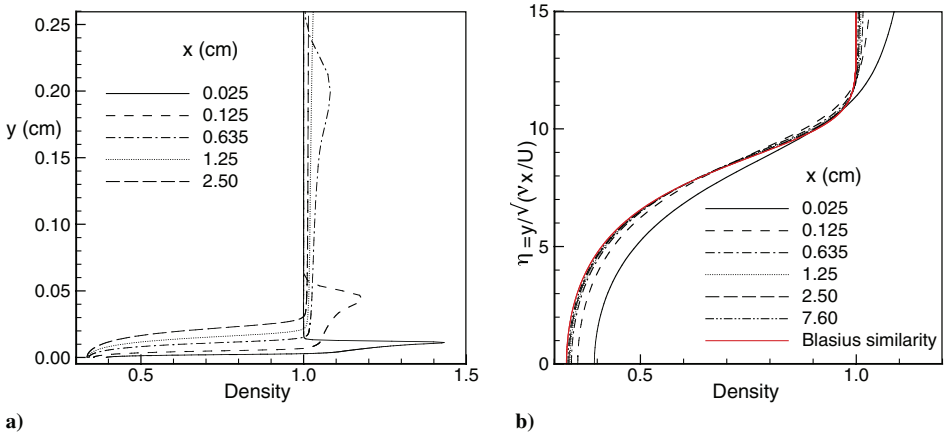

Fig. 5 Mean density profiles at different x locations.

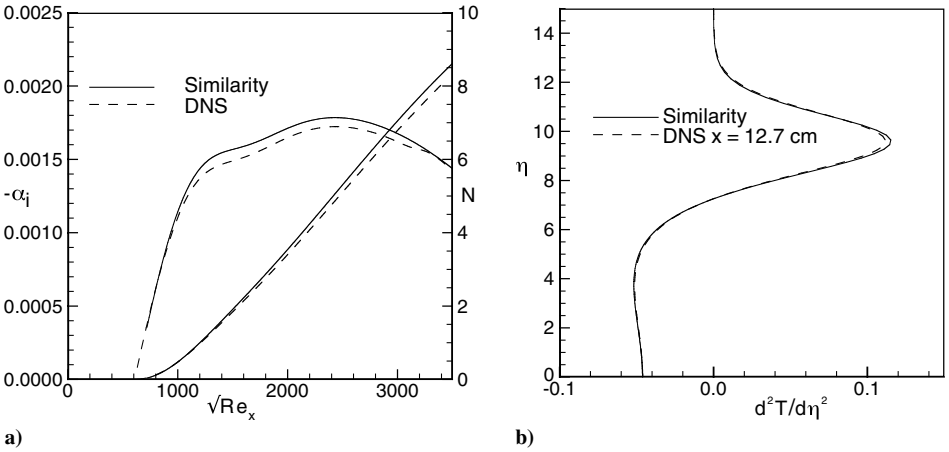

Fig. 6 (a) Comparison between the linear stability results computed using the Blasius similarity profiles and the profiles from the numerical solution. (b) Comparison of second derivatives for the temperature; (DNS denotes direct numerical simulation).

frequency and the spanwise wave number are $F = 1.25 * 10^{-5}$ and $\beta = 0.025$. These parameters give the largest N-factor close to the experimental transition location. To remain in the linear regime, very small initial amplitude of $\tilde{p}_{ac}/p_{\infty} = 1.0 * 10^{-7}$ is prescribed for the freestream acoustic waves. Even with these small initial amplitudes nonlinearity starts to develop near the end of the computational domain at $x \sim 25.0$ cm.

Figure 7 shows the results for the evolution of the unsteady fluctuations obtained from the simulation for the slow wave at a fixed time while Fig. 8 shows the disturbances for the fast wave. Figures 7a and 8a show the contours of the density fluctuations in the entire domain and Figs. 7b and 8b depict the results inside the boundary layer. In the density perturbations contour plot, Fig. 7b, the zero phase lines are marked to compare the wavelengths of the freestream acoustic oscillations and the oscillations inside the boundary layer that are generated by the diffraction of the acoustic waves across the leading edge. It is seen that starting from the leading-edge region the wavelengths of the oscillations inside the boundary layer are larger than the freestream acoustic oscillations. The perturbation field can be divided into four regions. One region is the area outside the shock where the acoustic waves propagate uniformly. The second region is the shock layer across which the acoustic waves are transmitted. The third region is the area between the shock and the boundary layer. This region consists of the transmitted external acoustic field and the

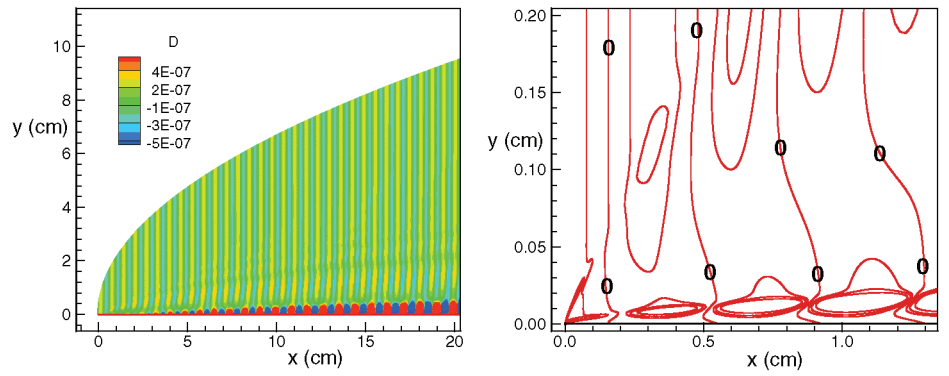

Fig. 7 Contours of the unsteady density fluctuations due to the interaction of a 3D slow acoustic wave with a flat plate with a blunted leading edge. $F = 1.25 * 10^{-4}$, $\beta = 0.025$, incident angle 0.0.

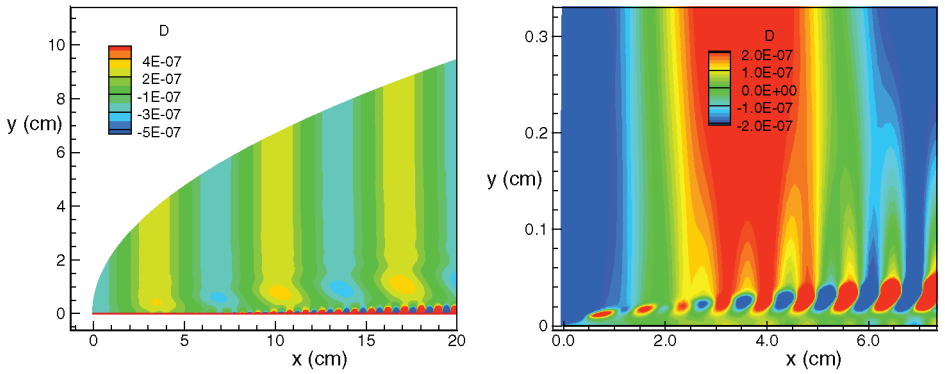

a) b)

Fig. 8 Contours of the unsteady density fluctuations due to the interaction of a 3D fast acoustic wave with a flat plate with a blunted leading edge. $F = 1.25 * 10^{-4}$, $\beta = 0.025$, incident angle 0.0.

disturbances that are radiated from the boundary layer. The fourth region is the boundary layer where the boundary-layer disturbances evolve. The figures show that the disturbances inside the boundary layer originate at the nose region. As noted earlier, the wavelength of the fast acoustic wave is about 10 times longer than that for the slow wave. An interesting observation, shown in Fig. 8b, is the appearance of short wavelength disturbances inside the boundary layer starting from the nose region.

As described earlier, grid refinement studies were performed with different grid distributions near the nose region. Figure 9 shows the pressure distribution along the wall obtained with different grids. Figure 10 shows the eigenfunction distributions near the wall and

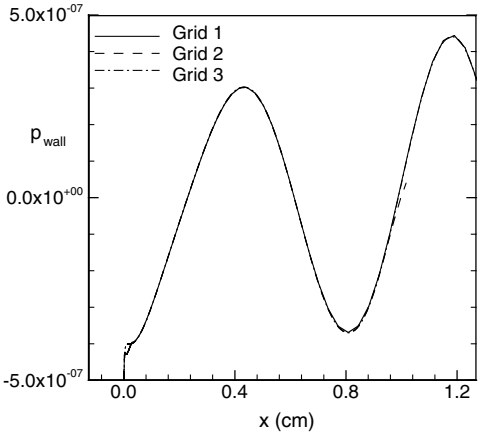

Fig. 9 Pressure fluctuations along the wall near the nose region for three different grids.

across the shock very near the nose region $x = 0.025$ and 0.50 cm. It is seen that all three computations give exactly the same results, except the shock becomes thinner with the fine grids, and confirm that the results obtained are not due to any numerical resolutions.

Figure 11 shows the instantaneous pressure fluctuations along the wall for the slow and fast waves and Fig. 12 shows the amplitude of the pressure fluctuations along the wall in a log scale. Figure 12 also includes the results from the parabolized stability equation (PSE) computations obtained for the same mean boundary-layer profiles. The figures clearly show the initial generation and the eventual exponential growth of the instability waves inside the boundary layer. The slow wave whose wavelength is closer to the wavelength of the instability wave transforms into instability waves smoothly. The fast waves whose wavelengths are much larger are initially modulated by short wavelength disturbances. Figure 11b also reveals that these short wavelength disturbances appear starting from the leading-edge region. This implies that when the fast acoustic waves are diffracted by the leading edge of the plate, disturbances with phase speed corresponding to the slow acoustic waves are also generated inside the boundary layer. These short waves transform into instability waves and grow exponentially downstream. The growth of the disturbances agrees very well with the PSE results about one acoustic wavelength downstream of the neutral point. Following the PSE results up to the neutral point, the initial amplitude of the instability waves at the neutral point can be estimated. From these values the receptivity coefficients can be evaluated. Specifically, the receptivity coefficient vaare completely diffracted by the leading edge of the plate disturbances with phase speed correspond to the slow acoustic wave is also generated inside the boundary l$C_{\text{recpt},p_{\text{wall}}}$ is defined by the initial amplitude of the pressure fluctuations at the wall at the neutral point nondimensionalized by the freestream acoustic pressure, that is,

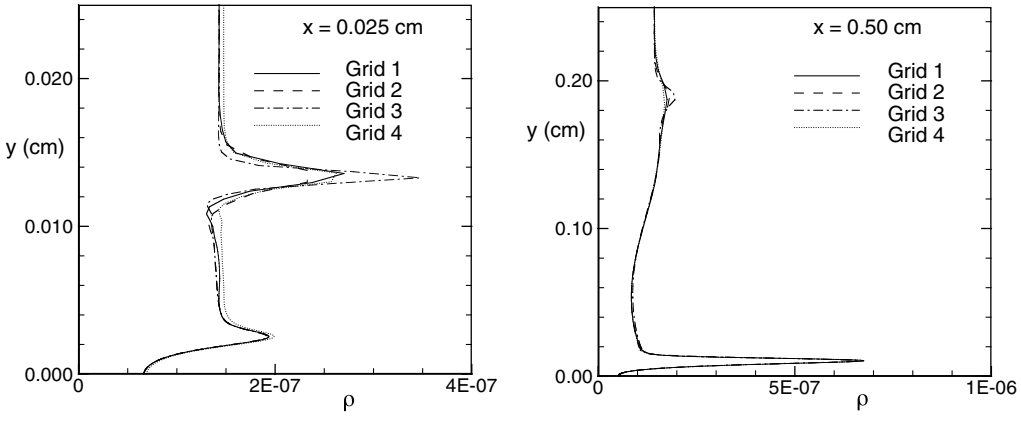

a) b)

Fig. 10 Eigenfunctions of the density fluctuations near the nose for three different grids.

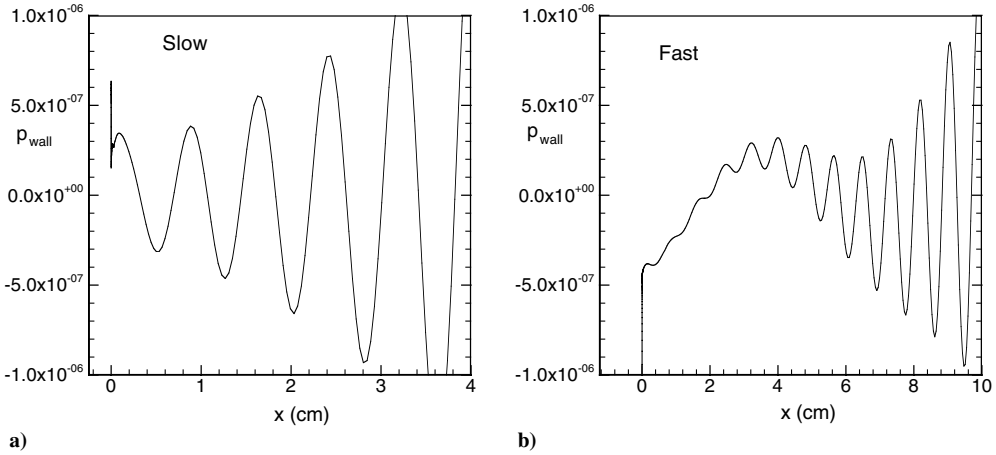

Fig. 11 Pressure fluctuations along the wall for the slow and the fast waves. $F = 1.25 * 10^{-4}$, $\beta = 0.025$.

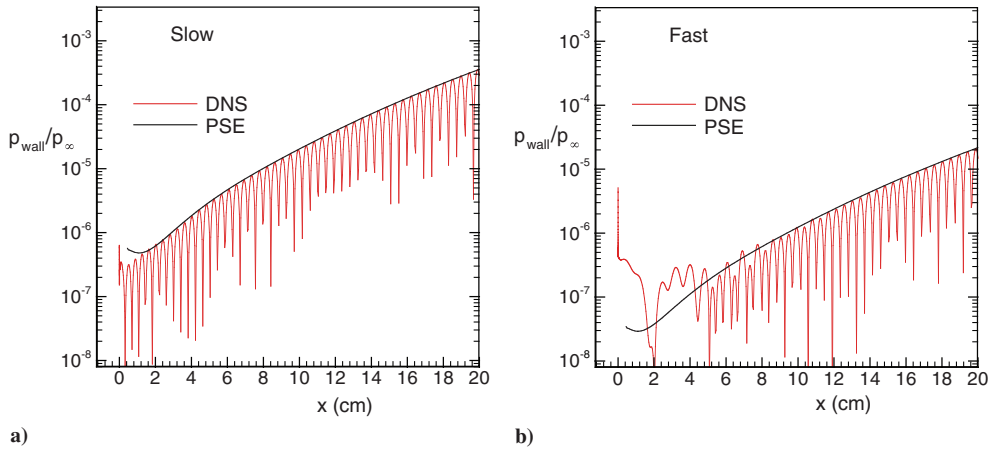

Fig. 12 Amplitude of the pressure fluctuation at the wall and comparison with the PSE. $F = 1.25 * 10^{-4}$, $\beta = 0.025$.

$$C_{\text{recpt},p_{\text{wall}}} = \frac{(p_{\text{wall}})_n}{p_{\text{ac}}} \tag{14}$$

The computed receptivity coefficients for the slow and fast waves are

$$C_{\text{recpt},p_{\text{wall}},S} = 1.20 \qquad C_{\text{recpt},p_{\text{wall}},F} = 0.07 \tag{15}$$

Similarly, the receptivity coefficients based on the maximum density fluctuations inside the boundary layer normalized by ρ_{ac} are calculated.

$$C_{\text{recpt},\rho_{\max},S} = 8.40 \qquad C_{\text{recpt},\rho_{\max},F} = 0.47 \tag{16}$$

The ratio of the receptivity coefficient between the slow and fast wave is about 17.0. As expected, the slow wave, whose phase speed is close to the neutral stability waves of the boundary layer, excites the instability waves more efficiently than the fast waves.

Figure 13 shows the wave number variation along the streamwise direction calculated from the unsteady fluctuations along the wall. This is achieved by first decomposing the fluctuations into harmonic components of the form

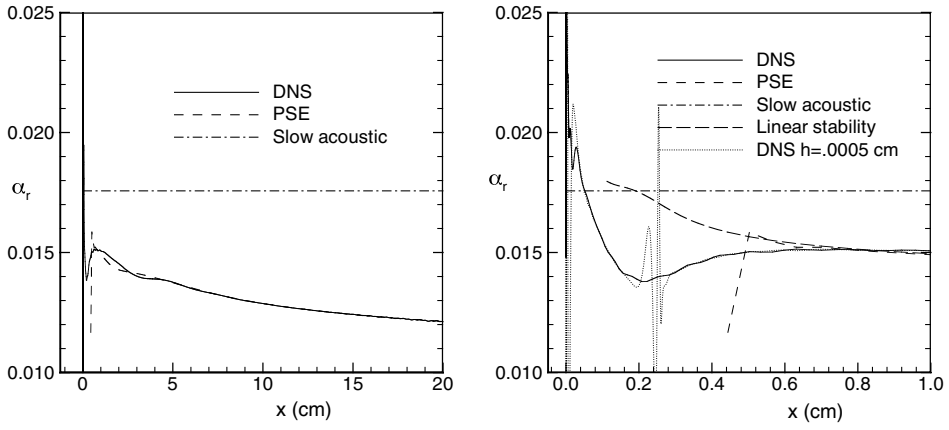

Fig. 13 Wave number of the pressure fluctuation at the wall and comparison with the PSE $F = 1.25 * 10^{-4}$, $\beta = 0.025$.

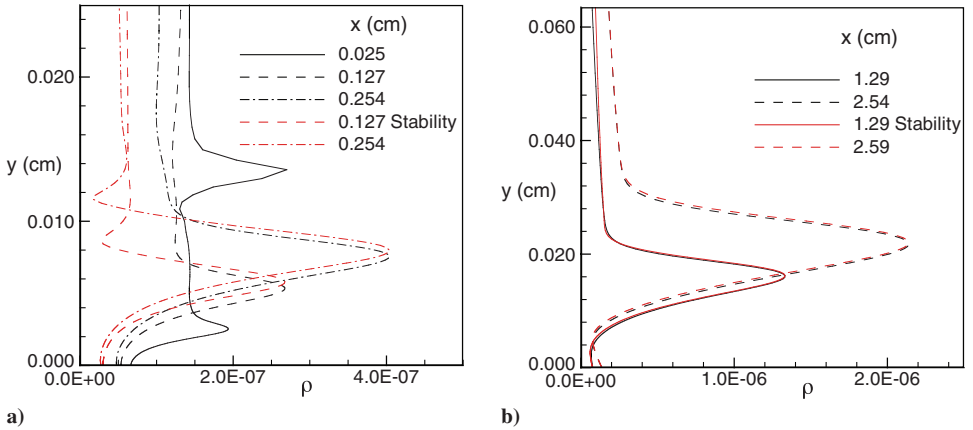

Fig. 14 Eigenfunctions of the density fluctuations and comparison with the linear stability calculations. $F = 1.25 * 10^{-4}$, $\beta = 0.025$.

$$p(x, z, t) = \tilde{p}(x)e^{i\beta z - i\omega t} + c.c. + \tilde{p}(x)e^{-i\beta z - i\omega t} + c.c. \qquad (17)$$

The wave number of the fluctuations are evaluated from the expression

$$\alpha(x) = \left(\frac{1}{i\tilde{p}(x)}\frac{\partial \tilde{p}(x)}{\partial x}\right) = \alpha_r + i\alpha_i \qquad (18)$$

Figure 13a shows the wave number distributions for the whole domain and Fig. 13b shows the results near the nose region for the slow wave. The figure includes the wave number distributions obtained from PSE computations and linear stability computations. The wave number of the slow acoustic wave is also drawn in the figure. Beyond the initial nose region $x > 0.75$ cm, the numerical wave number distribution agrees very well with the PSE and the linear stability results. The interesting part is how the slow acoustic wave with a higher wave number interacts and merges with the instability waves inside the boundary layer. This is clearly illustrated in Fig. 13b. The wave number near the nose region, as was observed in Fig. 7b, first decreases slowly up to $x \sim 0.25$ cm, it then increases slowly for $x > 0.25$ cm and merges with the T-S wave around $x \sim 0.75$ cm.

Figure 14 shows the eigenfunction distributions for the density fluctuations at different axial locations obtained from the simulation and the linear stability computations. Figure 14a shows the distributions near the nose region and Fig. 14b shows the results in the downstream region. Away from the nose region the computed eigenfunctions agree with the linear stability results and confirm the previous conclusions that the generated disturbances are in fact the T-S waves. Near the nose region the eigenfunctions differ from those for the instability waves and this region represents the interaction region.

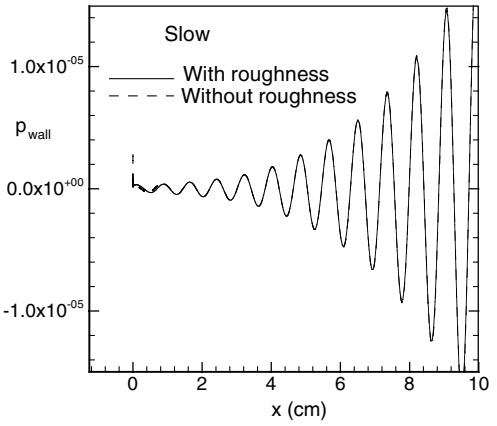

Fig. 15 Pressure fluctuations along the wall for the slow wave with and without roughness. $F = 1.25 * 10^{-4}$, $\beta = 0.025$.

Figure 15 shows the evolution of pressure fluctuations along the wall for the cases with and without the isolated roughness element. The computations are performed for $h = 0.0005$ cm, $\sigma = 5.0$, and $x_h = 0.25$ cm. This gives $h/\delta = 1/20$ and the width of the roughness is about two boundary-layer thicknesses at $x = x_h$. There are no noticeable differences between the two results, implying that the small isolated roughness elements do not enhance the instability waves, and the instability waves are basically generated by the interaction of acoustic waves with the leading-edge flow field. The variation of the wave number computed using Eq. (17) is also included in Fig. 13b. The wave number follows the same variation as in the no roughness case, except near the roughness. This confirms the conclusion that the roughness does not affect the receptivity process for these small roughness heights. However, a parametric study with different roughness shapes, heights, and distributions has to be conducted before making a firm conclusion.

IV. Conclusions

Because of the interaction of 3-D slow and fast acoustic disturbances with a blunted flat plate, and the evolution of disturbances inside the boundary layer, the boundary-layer receptivity process is numerically investigated at a freestream Mach number of 3.5 and at a high unit Reynolds number of $39.36 * 10^6$/m. The computations are performed with and without a 2-D isolated roughness element located near the leading edge. Both the steady and unsteady solutions are obtained by solving the full Navier-Stokes equations using the fifth-order accurate WENO scheme for space discretization and using third-order TVD Runge-Kutta scheme for time integration. At this Reynolds number, the neutral stability region occurs within about one to two acoustic wavelengths from the leading edge.

The mean flow computations show that the leading-edge shock is located upstream at about 1/6th of the thickness of the plate and the strength of the shock weakens within a short distance downstream. It is also noted that the boundary-layer profiles approach the similarity profiles within $x \sim 0.5$ to 1.0 in. from the leading edge. The linear stability and the N-Factor computations show that the stability characteristics of the computed and the similarity profiles are almost the same.

The simulation of the interaction of 3-D plane slow and fast acoustic waves with the boundary layer shows that the instability waves are generated very close to the nose region. The receptivity coefficients computed based on the pressure fluctuations at the wall at the neutral point are about 1.20 and 0.07 for the slow and fast acoustic waves, respectively. They are about 8.40 and 0.47 based on the maximum density fluctuations at the neutral point. This implies that the slow waves are more efficient, about 17 times, in generating instability waves inside the boundary layer than the fast waves.

The wave number distribution computed from the fluctuations inside the boundary layer revealed that initially, the wave number gradually decreases, starting from the leading edge, and becomes even smaller than the wave number for the instability waves. Further

downstream, it then increases and eventually becomes the same value as for the instability waves. The disturbances inside the boundary layer induced by the long wavelength fast acoustic waves are modulated by short wavelength disturbances starting from the leading edge. These short waves initiate the instability waves downstream.

The simulation results for the amplification of disturbances inside the boundary layer agree very well with the PSE results downstream of the neutral point. This implies that beyond the initial region the external forcing does not enhance or modify the amplitude of the instability waves. Simulation of the interaction of slow acoustic waves with an isolated 2-D roughness shows that small roughness elements do not enhance the amplitude of the instability waves.

The above findings suggest that in 2-D supersonic boundary layers the slow acoustic waves are the main catalyst in causing the transition. By knowing the approximate receptivity coefficients and the spectrum of the freestream slow acoustic disturbances, the initial amplitudes of the instability waves can be approximately prescribed, and linear and nonlinear PSE computations can be performed to predict the transition onset points accurately.

References

[1] Balakumar, P., "Transition in a Supersonic Boundary layer Due to Roughness and Acoustic Disturbances," AIAA Paper 2003-3589, 2003.

[2] Mack, L. M., "Boundary Layer Stability Theory," Jet Propulsion Laboratory, California Institute of Technology, JPL 900-277 Rev. A, Pasadena, Calif, Nov. 1969.

[3] Saric, W. S., Reed, H. L., and White, E. B., "Stability and Transition of Three-Dimensional Boundary Layers," *Annual Review of Fluid Mechanics*, Vol. 35, Jan. 2003, pp. 413–440. doi:10.1146/annurev.fluid.35.101101.161045

[4] Mack, L. M., "On the Application of Linear Stability Theory and the Problem of Supersonic Boundary-Layer Transition," *AIAA Journal*, Vol. 13, No. 3, 1975, 278–289. doi:10.2514/3.49693

[5] Gaponov, S. A., "Interaction Between a Supersonic Boundary Layer and Acoustic Disturbances," *Fluid Dynamics*, Vol. 12, No. 6, Nov. 1977, 858–862. doi:10.1007/BF01090319

[6] Gaponov, S. A., and Smorodsky, B. V., "Supersonic Boundary Layer Receptivity to Streamwise Acoustic Field," *IUTAM Symposium*, Spinger–Verlag, 1999. 223–228.

[7] Fedorov, A. V., and Khokhlov, A. P., "Excitation of Unstable Modes in a Supersonic Boundary Layer by Acoustic Waves," *Fluid Dynamics*, Vol. 26, No. 4, 1992, pp. 531–537. doi:10.1007/BF01050314

[8] Gaponov, S. A., "Excitation of Instability Waves in the Supersonic Boundary Layer by Sound," *IUTAM Symposium Potsdam*, Springer–Verlag, 1993, 206–212.

[9] Zhong, X., "Leading-Edge Receptivity to Free-Stream Disturbance Waves for Hypersonic Flow Over a Parabola," *Journal of Fluid Mechanics*, Vol. 441, 2001, pp. 315–367.

[10] Ma, Y., and Zhong, X., "Receptivity of a Supersonic Boundary Layer Over a Flat Plate. Part 2. Receptivity to Free-Stream Sound," *Journal of Fluid Mechanics*, Vol. 488, 2003, pp. 79–121. doi:10.1017/S0022112003004798

[11] Egorov, I. V., Fedorov, A. V., and Nechaev, A. V., "Recptivity of Supersonic Boundary Layers on a Blunt Plate to Acoustic Disturbances," AIAA Paper 2004-249, 2004.

[12] Kendall, J. M., "Wind Tunnel Experiments Relating to Supersonic and Hypersonic Boundary-Layer Transition," *AIAA Journal*, Vol. 13, No. 3, 1975, pp. 290–299. doi:10.2514/3.49694

[13] Semionov, N. V., Kosinov, A. D., and Maslov, A. A., "Experimental Investigation of Supersonic Boundary Layer Receptivity," *Transitional Boundary Layer in Aeroacoustics*, North–Holland, Amsterdam, 1996, pp. 413–420.

[14] Maslov, A. A., Sidorenko, A. A., Shiplyuk, A. N., and Arnal, D., "Leading Edge Receptivity of Hypersonic Boundary Layer on a Flat Plate," *Journal of Fluid Mechanics*, Vol. 426, 2001, pp. 73–94. doi:10.1017/S0022112000002147

[15] Chen, F. J., Malik, M. R., and Beckwith, I. E., "Comparison of Boundary Layer Transition on a Cone and Flat Plate at Mach 3.5," AIAA Paper 88-0411, 1988.

[16] Shu, C.-W., "Essentially Non-Oscillatory and Weighted Essentially Non-Oscillatory Schemes for Hyperbolic Conservation Laws," NASA/CR-97-206253 and ICASE Report No. 97-6, Nov. 1997.

[17] Atkins, H. L., "High-Order ENO Methods for the Unsteady Compressible Navier-Stokes Equations," AIAA Paper 91-1557, 1991.

[18] Balakumar, P., Zhao, H., and Atkins, H., "Stability of Hypersonic Boundary Layers Over a Compression Corner," AIAA Paper 2002-2848, 2002.

[19] Sesterhenn, J., "A Characteristic-Type Formulation of the Navier-Stokes Equations for High Order Upwind Schemes," *Computers & Fluids*, Vol. 30, No. 1, 2000, pp. 37–67. doi:10.1016/S0045-7930(00)00002-5

X. Zhong
Associate Editor